

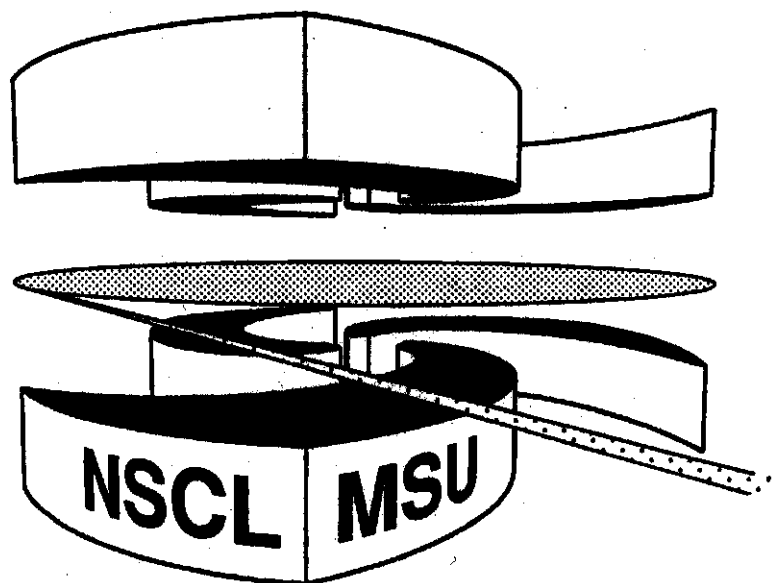


Michigan State University

National Superconducting Cyclotron Laboratory

**TWO-PROTON CORRELATION FUNCTIONS FOR $^{36}\text{Ar} + ^{45}\text{Sc}$
AT $E/A = 80 \text{ MeV}$**

**D.O. HANDZY, M.A. LISA, C.K. GELBKE, W. BAUER,
F.C. DAFFIN, P. DECOWSKI, W.G. GONG, E. GUALTIERI,
S. HANNUSCHKE, R. LACEY, T. LI, W.G. LYNCH, C.M. MADER,
G.F. PEASLEE, T. REPOSEUR, S. PRATT, A.M. VANDER MOLEN,
G.D. WESTFALL, J. YEE, and S.J. YENNELLO**



Two-Proton Correlation Functions for $^{36}\text{Ar} + ^{45}\text{Sc}$ at $E/A = 80$ MeV

D.O. Handzy, M.A. Lisa¹, C.K. Geibke, W. Bauer, F.C. Daffin, P. Decowski²,
W.G. Gong¹, E. Gualtieri, S. Hannuscbke, R. Lacey³, T. Li, W.G. Lynch, C.M.
Mader⁴, G.F. Peaslee⁴, T. Reposeur⁵, S. Pratt, A.M. Vander Molen, G.D. Westfall,
J.Yee, and S.J. Yennello⁶

*National Superconducting Cyclotron Laboratory and Department of Physics and
Astronomy Michigan State University, East Lansing, MI 48824, USA*

Abstract

Impact-parameter filtered longitudinal and **transverse** two-proton correlation functions measured for $^{36}\text{Ar} + ^{45}\text{Sc}$ collisions at $E/A = 80$ MeV are compared to predictions of the **BUU** transport model. For a cut on large transverse **energies**, the **overall** trends of the measured **correlation** functions are rather well reproduced by calculations for central **collisions**. Systematic discrepancies **become** visible, however, for calculations **with** larger impact parameters.

PACS number: 25.70.Pq

¹ Present address: Lawrence Berkeley Laboratory, Berkeley, CA 94720

² Present address: Department of Physics, Smith College, Northampton, MA 01063

³ Present address: Department of Chemistry, State University of New York, Stony Brook, NY 11776

⁴ Present address: Physics Department, Hope College, Holland, MI 49423

⁵ Present address: Laboratoire de Physique Nucléaire, Université de Nantes, Nantes Cedex 03, France

⁶ Present address: Cyclotron Institute, Texas A&M University, College Station, TX 77843

I. Introduction

Two-proton correlation functions at small relative momenta can probe the space-time characteristics of a reaction zone created in energetic nucleus-nucleus collisions, because the magnitude of nuclear and Coulomb final-state interactions, as well as anti-symmetrization effects, depend on the spatial separation of the two protons at the time of emission [1-34]. Correlation functions are evaluated as a function of q , the magnitude of the relative momentum vector $q = \frac{1}{2}(p_1 - p_2)$ in the proton-pair rest frame. The attractive S-wave nuclear interaction leads to a maximum in the correlation function at $q \approx 20$ MeV/c. Coulomb repulsion and anti-symmetrization produce a minimum at $q \approx 0$ [1].

The interpretation of correlation functions is complicated by the lack of a one-to-one relationship between space-time geometry of the source and the correlation function [4]. Model calculations simulating large sources of short lifetime can produce very similar correlation functions as model calculations simulating smaller sources of longer lifetimes [1,5]. This ambiguity between radius and lifetime can be resolved by employing cuts on the direction of relative motion [1,4,5,20,26,29,32]. For a source of finite lifetime, the phase space distribution of emitted particles shows an elongation in the direction of total momentum $P = p_1 + p_2$ (measured in the rest-frame of the emitting source). For such an elongated distribution, the Pauli anti-correlation will be greater when the relative momentum is in the transverse (non-elongated) direction as compared with the longitudinal (elongated) direction. Therefore, transverse correlation functions ($q \perp P$) will be suppressed as compared to longitudinal correlation functions ($q \parallel P$) [4,5,26,32].

The dependence of the correlation function on the total momentum of the pair provides valuable information on the temporal evolution of the reaction

zone and may be sensitive to emission and expansion time scales [2-7]. Previous measurements of two-proton correlation functions at bombarding energies between $E/A \approx 20$ and 100 MeV found stronger correlations at $q \approx 20$ MeV/c for protons emitted with higher energy [11,13,19-31], indicating that high-energy protons were emitted from smaller sources (or with shorter characteristic time scales) than low-energy protons. Impact parameter averaged data at these energies could be understood rather well in terms of calculations which solve the Boltzmann-Uehling-Uhlenbeck (BUU) transport equation [5,7,19,25,26]. However, a discrepancy with this trend was reported at a higher energy, $E/A=200$ MeV, where the measured two-proton correlation function showed little dependence on the proton energy [30].

BUU transport model calculations predict a strong dependence of the two-proton correlation function on the impact parameter of the collision [5]. In this work, we investigate the dependence of impact-parameter selected two-proton correlation functions upon the magnitude and on the relative orientation of the total and relative momentum vectors, P and q , and we compare these data to predictions of the BUU transport theory. Some aspects of this work were published previously [31,32].

II. Experimental Details

The experiment was performed at the National Superconducting Cyclotron Laboratory at Michigan State University. From the K1200 cyclotron, a beam of ^{36}Ar ions, at $E/A=80$ MeV incident energy, was focused on a ^{45}Sc target of area density 10.0 mg/cm². Beam intensities were typically 3×10^8 particles/sec. Charged particles were observed in 209 plastic E- ΔE phoswich detectors of the MSU 4π Array [35], covering polar angles between 7° and 158° in the laboratory frame. Specifically, the 4π Array was made up of a forward pentagon (the

"Forward Array") consisting of 45 phoswich detectors covering laboratory polar angles between 7° and 18° with a geometrical efficiency of about 56%, and the "Ball" portion consisting of 164 plastic phoswich detectors covering polar angles between 23° and 158° with an efficiency of approximately 85%. Particles which stopped in the slow (E) plastic scintillators were identified by particle type and energy, with energy resolution of about 10%. Energy thresholds for protons and carbon ions, respectively, were approximately 17 and 32 MeV/nucleon in the ball detectors, and 12 and 22 MeV/nucleon in the Forward Array. The fast rise time of the 4π Array phototubes made elimination of random hits from different beam bursts possible through 1-dimensional time cuts.

One hexagonal module of the 4π Array (centered at $\theta_{\text{lab}} = 38^\circ$) was replaced with a 56-element high-resolution hodoscope, described in detail in refs. [26,36,37]. Each element of the hodoscope consisted of a 300 μm thick planar surface-barrier silicon detector, backed by a 10-cm long cylindrical CsI(Tl) crystal read by a PIN diode. Each telescope subtended a solid angle of approximately $\Delta\Omega \approx 0.37$ msr. The angular coverage of each telescope is shown in Fig. 1, where θ and ϕ denote the polar and azimuthal angles of the detectors with respect to the beam axis. The nearest neighbor spacing between telescopes was about 2.6° . Energy calibration of the CsI(Tl) detectors was performed by scattering α -particles of incident energy $E/A=25, 30,$ and 40 MeV from Au and polypropylene targets, while the Si detectors were calibrated with a precision pulser. Energy calibrations were linear, with an energy resolution of about 1% for 50 MeV protons. Detection thresholds for protons were typically 8 MeV. Random coincidences from different beam bursts were easily identified through relative timing spectra after rise-time effects were accounted for off-line.

During the experiment, both two-proton coincidences and single-proton events in the hodoscope were recorded in coincidence with the corresponding data from the 4π Array. Events which triggered the 4π Array but not the hodoscope were rejected by a fast-clear circuit, which was necessary because the CsI(Tl) detectors of the hodoscope have a much longer rise time than the fast plastic scintillators of the 4π Array. The construction of an impact parameter filter requires "minimum bias" data (see section III) from the 4π Array; such data were collected through a third trigger requiring the detection of at least one particle in the 4π Array.

III. Impact Parameter Selection

Models of nuclear collisions make specific predictions for fixed impact parameter or entrance-channel angular momentum, but data sample a range of impact parameters. When comparing model predictions with data, one must account for the impact parameter distribution sampled by the data and investigate the associated uncertainties.

Following refs. [38,39], we construct a reduced impact parameter scale by means of the geometric relation

$$\hat{b}(X) = \left(\int_X^{\infty} \frac{dP(X')}{dX'} dX' \right)^{1/2}. \quad (1)$$

In Eq. 1, $dP(X)/dX$ is the normalized probability distribution for a suitably chosen observable X , such as the charged particle multiplicity N_C , the mid-rapidity charge Z_y , or the transverse energy E_T . (In order to reduce the effects of "self-cut" biasing, particles detected in the 56 element hodoscope were not included in our definitions of X .) If the observable X exhibits a strictly monotonic dependence upon impact parameter b , then $\hat{b}(X) = b(X) / b_{\max}$, where b_{\max} is the

maximum impact parameter for which the measured value of X assumes a non-zero value.

In the present analysis, we construct an impact parameter filter by cuts on the total transverse energy which exhibit good selectivity for central collisions [38,39],

$$E_t = \sum_i E_i \sin^2(\theta_i), \quad (2)$$

where E_i and θ_i denote the laboratory kinetic energy and polar angle of particle i , detected in the 4π Array. This definition of E_t is consistent with that used in previous analyses [31,32,37,38]. It is appropriate at nonrelativistic energies since $E \sin^2 \theta = p_{\perp}^2 / 2m$ provides a measure for energy dissipation into velocity components perpendicular to the beam axis.

Figure 2 illustrates the relationship between E_t and $\hat{b}(E_t)$ defined by Eq. 1. The top panel shows the transverse energy spectrum dP/dE_t , measured for the minimum bias trigger (at least one detector firing in the 4π Array), and the bottom panel shows the function $\hat{b}(E_t)$.

Through the relationship $\hat{b}(E_t)$, any distribution dP/dE_t can be transformed into a reduced impact parameter distribution using

$$\frac{dP}{db} = \frac{dP}{dE_t} \left/ \frac{d\hat{b}}{dE_t} \right. \quad (3)$$

Figure 3 presents the reduced impact parameter distributions corresponding to the different experimental triggers. The solid line represents the minimum bias trigger which, by construction, increases linearly with \hat{b} . The dot-dashed and dashed lines show the distributions for single and two-proton inclusive events in the 56-element hodoscope, respectively. Requiring one or more protons in the hodoscope clearly biases the data to more central collisions.

In Fig. 4, we compare the transverse energy spectrum to predictions of the BUU transport model using a geometric weighting of impact parameters. Since the BUU model only predicts the emission of nucleons, Fig. 4 shows the predicted values of E_t when neutrons are included (dashed line) and not included (dot-dashed line) in the definition of E_t . The obvious disagreement between observed and calculated E_t -spectra arises primarily from the fact that the BUU transport model describes the time evolution of the single-particle phase-space distribution. As a consequence, the model cannot reproduce observables sensitive to the emission of complex fragments contributing to the experimental sum in Eq. 2. (Similar difficulties are encountered for other observables, such as N_C or Z_Y .) Since the calculations fail to reproduce the observed E_t spectrum, comparisons of E_t -selected data to model predictions are not straightforward. Clearly, the use of identical E_t -cuts on data and theoretical predictions is inappropriate. We will consider two alternative approaches to overcome this difficulty.

First, we define "equivalent" E_t -cuts for measured and calculated events by adopting equivalent geometrical interpretations of measured and calculated E_t distributions, i.e. by defining a relation $\hat{b}'(E_t^{BUU})$ for BUU events as we have done for the data and applying the same cuts on $\hat{b}'(E_t^{BUU})$ and on $\hat{b}(E_t^{exp})$. Equivalent experimental and theoretical cuts, at E_t and \hat{E}_t , produce the same reduced impact parameters if

$$\int_{E_t}^{\infty} dE'_t \frac{dP(E'_t)}{dE'_t} = \int_{\hat{E}_t}^{\infty} dE'_t \frac{d\hat{P}(E'_t)}{dE'_t}. \quad (4)$$

In Eq. 4, dP/dE_t and $d\hat{P}/dE_t$ denote the experimental and theoretical E_t -distributions, respectively. One may expect that equivalent E_t -cuts select comparable distributions of the true impact parameter in the data and in the

calculations. Calculations performed by this prescription will be termed "E_t-selected".

As an alternative, we attempt to reconstruct a realistic impact parameter distribution sampled by the data. For this purpose, we employ alternative reduced impact parameter scales derived from the charged-particle multiplicity and mid-rapidity charge (using $X = N_C$ and Z_Y , respectively, in Eq. 1). The mid-rapidity charge, Z_Y , is defined by

$$Z_Y = \sum_{i=1}^{N_f} Z_i \cdot \Theta(y_i - 0.75y_{\text{targ}}) \cdot \Theta(0.75y_{\text{proj}} - y_i) \quad (5)$$

where $\Theta(x)$ is the Heaviside function and y_{targ} , y_{proj} , and y_i are, respectively, the rapidity of target, projectile, and the i^{th} charged particle in the center-of-momentum frame of the system.

By construction, a sharp cut in the observable X corresponds to a sharp cut in $\hat{b}(X)$. In order to quantify the values of impact parameter that are sampled in the data, one must consider the effects of fluctuations in the relationship between the true impact parameter of a collision and the global observable X . Following refs. [38,39], we obtain an estimate of the scale of the fluctuations in the relationship between the true reduced impact parameter \hat{b}_{true} and the transverse energy E_t by observing the effect of narrow cuts in $\hat{b}(N_C)$ and $\hat{b}(Z_Y)$ on the distribution $dP/d\hat{b}(E_t)$. The upper panel of Fig. 5 shows $dP/d\hat{b}(E_t)$ for narrow central cuts in $\hat{b}(N_C)$ (dashed line) and $\hat{b}(Z_Y)$ (dot-dashed line), and for a double-cut on both variables (solid line). Similar distributions are shown in the lower panel for somewhat less central cuts. The widths $\sigma(\hat{b})$ of the double-cut distributions can be taken as upper limits of the widths of the distribution of the true reduced impact parameter for a given value of E_t [38].

To obtain a realistic "true" reduced impact parameter distribution $dP/d\hat{b}_{true}$, it is necessary to fold the effects of the finite widths into the impact parameter distribution. As an ansatz, we take the following expression for the probability distribution of true impact parameters for events filtered by a sharp cut on $\hat{b} \equiv \hat{b}(E_t)$:

$$\frac{dP(\hat{b}; \hat{b}_{true})}{d\hat{b}_{true}} \propto \hat{b}_{true} \cdot \exp\left(-\frac{(\hat{b}_{true} - \hat{b})^2}{\sigma^2(\hat{b})}\right) \cdot \Theta(1 - \hat{b}_{true}) \cdot \Theta(\hat{b}_{true}). \quad (6)$$

For a given cut $E_t^{\min} \leq E_t \leq E_t^{\max}$, the true reduced impact parameter distribution is then given by

$$\frac{dP}{d\hat{b}_{true}} = \int_{\hat{b}_{\min}}^{\hat{b}_{\max}} d\hat{b} \left[\frac{dP(\hat{b}; \hat{b}_{true})}{d\hat{b}_{true}} \cdot \frac{dP(\hat{b})}{d\hat{b}} \right], \quad (7)$$

with $\hat{b}_{\min} = \hat{b}(E_t^{\max})$ and $\hat{b}_{\max} = \hat{b}(E_t^{\min})$. By inserting the geometric distribution, $dP/d\hat{b} = 2\hat{b}/\hat{b}_{\max}^2$, into Eq. 7, we constructed explicit impact parameter distributions used to weight the impact parameters of BUU calculations. (In our BUU calculations, we assumed $b_{\max} = 10$ fm; an additional requirement of proton emission in the direction of the hodoscope was imposed when selecting phase space points for the calculation of correlation functions.) Calculations performed with this prescription will be termed " \hat{b} -selected".

For illustration, the upper panel of Fig. 6 shows the sharp cuts in $\hat{b}(E_t)$ used in our analysis of central and peripheral collisions. The lower panel shows the corresponding distributions $dP/d\hat{b}_{true}$, extracted via Eqs. 6 and 7.

IV. Calculation of Correlation Functions

Theoretical correlation functions were calculated using the Koonin-Pratt formalism [4,5]. In these calculations, the one-body phase space density distribution provided by the BUU is convoluted with the two-proton wave

function. In the present analysis, we use the BUU model of Bauer [7,40-43] with a stiff equation of state ($K=380$ MeV) and with the nucleon-nucleon cross section set to its free value. A proton was considered "emitted" if its local density was one-eighth that of normal nuclear matter at a time $t < t_{\text{cut}} = 150$ fm/c and if it did not reenter a region of higher density until the calculation was terminated at $t_f = 200$ fm/c. Some theoretical uncertainty exists with respect to the particular choice of $t_{\text{cut}} = 150$ fm/c which was done for the sake of consistency with previous model predictions [5,25,26,31].

To simulate a geometric distribution of impact parameters, N_b , the number of ensembles (or simulated events) with a given impact parameter b was set proportional to b . With n , the event number running from 1 to N_b and i , the particle number, running from 1 to $M_{n,b}$ (the multiplicity of the event), the correlation function was calculated as:

$$1 + R(q) =$$

$$C \frac{\sum_b \frac{1}{N_b} \sum_{n_1}^{N_b} \sum_{n_2}^{N_b} \sum_i^{M_{n_1,b}} \sum_j^{M_{n_2,b}} (1 - \delta_{ij} \delta_{n_1 n_2}) \delta_{\Delta} \left(q - \frac{|p'_{i,b}{}^{n_1} - p'_{j,b}{}^{n_2}|}{2} \right) \left| \Phi \left(x_{i,b}{}^{n_1} - x_{j,b}{}^{n_2}; \frac{|p'_{i,b}{}^{n_1} - p'_{j,b}{}^{n_2}|}{2} \right) \right|^2}{\sum_{b_1} \sum_{b_2} \sum_{n_1}^{N_{b_1}} \sum_{n_2}^{N_{b_2}} \sum_i^{M_{n_1,b_1}} \sum_j^{M_{n_2,b_2}} (1 - \delta_{ij} \delta_{n_1 n_2} \delta_{b_1 b_2}) \delta_{\Delta} \left(q - \frac{|p'_{i,b_1}{}^{n_1} - p'_{j,b_2}{}^{n_2}|}{2} \right)} \quad (8)$$

Here, the primed momenta are calculated in the center-of-momentum frame of the proton pair and the double-primed coordinates are calculated in the center-of-momentum frame at the time of emission of the second particle; Φ is the wavefunction of relative motion between the two protons; $\delta_{\Delta}(q)$ is the "binning function" which is unity for $|q| \leq \frac{1}{2} \Delta$ and zero otherwise; C is a normalization constant.

Construction of the correlation function with the E_T -selected technique involves setting N_b proportional to b , and limiting the sums in Eq. 8 to include

only those events with E_t in the desired range. Construction of the correlation function with the \hat{b} -selected technique involves setting N_b proportional to the distribution $dP/d\hat{b}_{true}$ shown in the bottom of Fig. 6.

V. Construction of Experimental Correlation Functions

Experimentally, the two-proton correlation function, $1+R(q)$, is defined through the relation

$$\sum Y_2(\mathbf{p}_1, \mathbf{p}_2) = N(1 + R(q)) \sum Y_{back}(\mathbf{p}_1, \mathbf{p}_2) \quad (9)$$

where $Y_2(\mathbf{p}_1, \mathbf{p}_2)$ is the measured coincidence yield for two protons with momenta \mathbf{p}_1 and \mathbf{p}_2 , and $Y_{back}(\mathbf{p}_1, \mathbf{p}_2)$ is the background yield. In our analysis, we adopted the singles technique for the construction of the background yield, $Y_{back}(\mathbf{p}_1, \mathbf{p}_2) = Y_1(\mathbf{p}_1) \cdot Y_1(\mathbf{p}_2)$, where $Y_1(\mathbf{p})$ is the measured singles yield for a proton of momentum \mathbf{p} . As a check, we have also constructed background yields via the event-mixing technique [44] in which the background yield is constructed by mixing two protons from different coincidence events. Differences between correlation functions constructed by the singles and event-mixing techniques were found to be of the order of statistical uncertainties, with a slight damping in the correlations observed for the event-mixing technique. This observation is consistent with previous studies [44]. A large difference between the two techniques is not expected because the coincidence and singles data sample very similar ranges of impact parameter (see Fig. 3). For impact-parameter selected correlation functions, possible differences in impact-parameter weights of single and two-proton events in the hodoscope are reduced even further.

The summations in Eq. 9 are over events selected by the specified cuts on E_t , on the magnitude of the total laboratory momentum, $P_{lab} = |\mathbf{p}_{1,lab} + \mathbf{p}_{2,lab}|$, and on the relative angle, $\psi = \cos^{-1}(|\mathbf{p} \cdot \mathbf{q}| / Pq)$, between the total and relative

momenta, P and q . (The cuts on ψ will be defined in different rest frames, specified below.) The correlation function will be evaluated as a function of the magnitude of the relative momentum q of the proton pair, and the normalization constant N is evaluated for the ψ -integrated correlation function such that $R(q)=0$ for large q , where final state interactions are believed to be negligible.

VI. Angle Integrated Correlation Functions

Angle-integrated correlation functions measured in the present experiment were published in ref. [31] and compared to predictions with the BUU transport model using the E_T -selected method. Figure 7 summarizes the main findings of ref. [31]. The solid points in the figure show the measured [31] total momentum dependence of the average height, $\langle 1+R \rangle_{15-25 \text{ MeV}/c}$ of the two-proton correlation function in the peak region at $q \approx 20 \text{ MeV}/c$. For relatively small sources and short emission time scales, this quantity is the primary indicator of the extent of the phase-space distribution of emitted protons. Error bars indicate statistical uncertainties as well as an estimate of the normalization uncertainty in the high- q region. For orientation, the right-hand axis gives the Gaussian radius of a zero-lifetime spherical source that produces a correlation function with the same value of $\langle 1+R \rangle_{15-25 \text{ MeV}/c}$. Impact-parameter filtered BUU-predictions are represented by open symbols. The open squares show the results of E_T -selected calculations (published previously [31]), and the open circular points show the results of \hat{b} -selected calculations. The two calculations produce very similar results: for central collisions (top panel), the agreement between experimental and theoretical correlation functions is satisfactory, but for peripheral collisions (bottom panel), the BUU transport theory underpredicts the total momentum dependence of the correlation function.

The \hat{b} -selection method is computationally more efficient than the E_T -selection method. For E_T -selected calculations, the impact parameters are initially chosen according to an unbiased geometrical distribution, and the calculated events are then selected by the appropriate cuts on E_T , i.e. not all BUU events are used for further analysis. For \hat{b} -selected calculations, on the other hand, the impact parameters are initially chosen according to the impact parameter distribution $dP/d\hat{b}_{true}$ shown in the bottom of Fig. 6 with all BUU events being used for further analysis. Since both methods give rather similar results, we will adopt the more efficient \hat{b} -selection method for the remainder of this paper.

The dynamics of strictly central ($\hat{b} = 0$) collisions cannot be investigated experimentally since contributions from non-zero impact parameters cannot be avoided. Nevertheless, it is interesting to investigate theoretical predictions for this idealized case and to assess the significance of imperfect impact parameter selection. For this purpose, we also present BUU predictions for $\hat{b} = 0$ (shown by solid diamond-shaped symbols in the upper panel of Fig. 7). As may be expected, the removal of non-central collisions from the calculations leads to an enhanced momentum dependence of the two-proton correlation function. While the agreement with the data is somewhat worse than for the more realistically filtered calculations, the qualitative observation of a strong momentum-dependence of two-proton correlation functions for central collisions is already rather well reproduced in these simplified $\hat{b} = 0$ calculations.

The success of the BUU model in predicting the strong momentum dependence of the two-proton correlation functions observed in near-central collisions (top panel of Fig. 7) suggests that the BUU transport model provides a reasonable description of the phase-space density-distribution of nucleons

emitted in collisions at small impact parameter. Predictions for peripheral collisions may be less reliable [45].

In the following, we will investigate data and theoretical predictions for near-central collisions in more depth by exploring two-proton correlation functions with cuts on the angle ψ between P and q .

VII. Longitudinal and Transverse Correlation Functions

"Angle-integrated" correlation functions (no explicit cuts on the angle ψ between P and q) probe the volume of the phase space distribution of emitted particles with little sensitivity to its shape [4,5]. Without independent knowledge of the size of the emitting system and the emission mechanism (e.g. surface versus volume emission) "angle-integrated" correlation functions are incapable of discriminating between smaller sources of longer lifetime and larger sources of shorter lifetime.

This space-time ambiguity may be reduced by analyzing two-proton correlation functions with cuts on the angle $\psi = \cos^{-1}(|P \cdot q| / Pq)$ between P and q [1,4,5,20,29,32,33]. Emission from a long-lived source leads to a phase-space distribution elongated in the direction of P , the total momentum of the proton pair with respect to the rest frame of the emitting source. The magnitude of this elongation is of the order of $P\tau/2m$ where τ is the average time interval between the emissions of the detected particles. Two-proton correlation functions exhibit a directional sensitivity primarily due to an increased Pauli suppression in the non-elongated (transverse) direction. (For very extended phase-space distributions, the Coulomb interaction causes additional ψ -dependencies [5,46].) For long-lived sources, transverse correlation functions ($q \perp P$) are therefore suppressed at small q in comparison with longitudinal correlation functions ($q \parallel P$). Since the total momentum, P , depends on the rest frame of the source,

but the relative momentum, q , does not, the angle ψ , and hence the definition of longitudinal and transverse cuts, depends on the rest frame of the emitting system. Care must be taken to characterize the rest frame of the emitting source [29,32,33].

Longitudinal and transverse correlation functions of low-energy proton pairs ($P_{\text{lab}} = 400\text{-}600$ MeV/c) emitted in central $^{36}\text{Ar} + ^{45}\text{Sc}$ collisions have already been published in ref. [32]. Significant differences were observed, when the longitudinal ($\psi_{\text{long}} = 0^\circ\text{-}50^\circ$) and transverse ($\psi_{\text{trans}} = 80^\circ\text{-}90^\circ$) cuts were defined in the $^{36}\text{Ar} + ^{45}\text{Sc}$ center-of-momentum frame. These differences were largely washed out when the longitudinal and transverse cuts were defined in the laboratory rest frame. These observations could be reproduced by adopting a simple source parametrization simulating emission from a source of finite lifetime $\tau = 20\text{-}40$ fm/c and spherically symmetric Gaussian density profile, $\rho(r) \propto \exp(-r^2/r_0^2)$ with $r_0 = 4.5\text{-}4.8$ fm, moving with the center-of-momentum frame of reference. Energy and angular distributions of the emitted protons were selected by randomly sampling the experimental yield. In this section, we will investigate whether the observed directional dependence of the two-proton correlation function can be understood in terms of the phase space distribution predicted by the BUU transport model using the parameters described in Section IV.

The solid and open points in Fig. 8 show the longitudinal and transverse correlation functions measured for central $^{36}\text{Ar} + ^{45}\text{Sc}$ collisions, with the cuts on the angle ψ being defined in the center-of-momentum frame of projectile and target. The central cuts correspond to $\hat{b}(E_i) \leq 0.36$. The top panel of the figure shows previously published [32] results for low energy particles, $P_{\text{lab}} = 400\text{-}600$ MeV/c, and the bottom panel shows previously unpublished results for the

emission of more energetic particles, $P_{\text{lab}} = 700\text{-}1400$ MeV/c. (For consistency with refs. [31,32], we define the cuts on the magnitude of the total momentum in the laboratory rest frame, but we will use different rest frames for the definition of the angle ψ .) Significant differences between longitudinal and transverse correlation functions are observed for the emission of low-energy particles, $P_{\text{lab}} = 400\text{-}600$ MeV/c, but not for the emission of high-energy particles, $P_{\text{lab}} = 700\text{-}1400$ MeV/c, likely reflecting decreasing emission time-scales for particles of increasing energy.

For orientation, the solid and dashed curves in Fig. 8 show longitudinal and transverse two-proton correlation functions predicted by BUU calculations for the idealized case of strictly central collisions, $\hat{b} = 0$. The calculations reproduce magnitude and difference between longitudinal and transverse correlation functions rather well, slightly overpredicting the height of the peak at $q = 20$ MeV for high-energy protons, $P_{\text{lab}} = 700\text{-}1400$ MeV/c. This latter discrepancy was already visible in Fig. 7. It is comparable in magnitude [5] to the theoretical uncertainty due to our choice of emission criteria, $t_{\text{cut}} = 150$ fm and $\rho < \rho_0/8$. Calculations using $t_{\text{cut}} = 200$ fm/c predict slightly reduced correlation functions: they agree rather well with the data for the high-momentum gate, $P_{\text{lab}} = 700\text{-}1400$ MeV/c, but they underpredict the maximum at $q = 20$ MeV/c, and they predict too large a split between longitudinal and transverse correlation functions.

Figure 9 shows results for calculations which incorporate the effects due to the finite resolution of the centrality filter via the \hat{b} -selection method. These more realistic calculations reproduce the overall trends of the data rather well with a slight overprediction of the difference between longitudinal and transverse correlation functions for the high-momentum gate, $P_{\text{lab}} = 700\text{-}1400$ MeV/c (bottom panel of Fig. 9).

In order to provide more insight into the transport model predictions, we show in Fig. 10 the acceptance of the hodoscope in the p_x vs. p_z plane for single-proton momentum cuts of $p_{lab} = P_{lab}/2$. The dashed lines indicate the angular acceptance of the hodoscope, $\theta_{lab} = 30^\circ - 45^\circ$. The dotted and hatched areas depict cuts corresponding to $P_{lab} = 400-600$ MeV/c and $P_{lab} = 700-1400$ MeV/c. For reference, the two solid circles depict the Fermi momentum spheres of projectile (centered at $p_z/A = 395$ MeV/c) and target (centered at $p_z = 0$), and the dashed circle depicts the region of final momenta accessible by single nucleon-nucleon scattering processes, representative of a mid-rapidity source (centered at $p_z/A = 197$ MeV/c). The low momentum cut, $P_{lab} = 400-600$ MeV/c, selects protons emitted at large transverse angles with low energies with respect to the center-of-momentum rest frame for projectile and target. This kinematic region should be strongly populated by emission from the cooling participant zone formed by the geometrical overlap of projectile and target, and the simple concept of emission from a source at rest in the center-of-momentum frame of projectile and target may be well justified for central collisions. In contrast, the high momentum cut, $P_{lab} = 700-1400$ MeV/c, selects fast particles with velocities closer to the projectile than target velocity. In this kinematic domain, contaminating emission from excited projectile spectator matter is likely to occur, especially when contributions from non-central collisions exist. Here, the concept of emission from a single source, at rest in the center-of-momentum frame of projectile and target, may become inappropriate.

We will explore alternative choices of rest-frames for the definition of ψ further below. First, however, we illustrate the non-trivial relationship between the space-time evolution of the emitting source and the phase-space distribution of emitted particles for the simplified case of emission of low-energy protons in central collisions. Figure 11 depicts four snapshots in time of the spatial

distribution of "detected" particles (light points) and of the residual system (heavy points). The distributions are depicted in the center-of-momentum frame of projectile and target with the coordinate system chosen to have the relative velocity of projectile and target parallel to the z-axis and the center of the 56-element hodoscope in the (x,z)-plane. "Detected" particles (light points) represent particles emitted prior to the time indicated in each of the panels; the momenta of these particles are further required to be within the angular acceptance of the hodoscope and have the magnitude $p_{\text{lab}} = 200 \pm 5 \text{ MeV}/c$. The arrows indicate the direction of motion of representative particles. The residual system (heavy points) is defined by the requirement $\rho \geq \frac{1}{8}\rho_0$. The figure shows the (x,z)-projection of particles which lie within $\pm 3 \text{ fm}$ of the (x,z)-plane, $|y| < 3 \text{ fm}$.

The residual system is predicted to evolve into a relatively long-lived toroidal configuration depicted in this presentation by two nearly circular density distributions to the left and right of the symmetry axis, $z = 0$. (The toroidal shape of the residual system has been verified by making various other projections, not shown here for the sake of brevity.) Such toroidal distributions have been predicted for a variety of other system at comparable incident energies per nucleon [47-50], but concrete experimental evidence for the existence of such distributions does not yet exist.

The phase space distribution of detected particles exhibits a clearly non-spherical shape, consistent with the experimentally observed difference between longitudinal and transverse correlation functions. (The finite width of the cut $p_{\text{lab}} = 200 \pm 5$, introduces a small ($\approx 2 \text{ fm}$) artificial elongation of the depicted phase space distribution which is superimposed on the elongation caused by different emission times.) While consistent with the BUU predictions for central collisions, the present correlation functions must not be construed as experimental

confirmation of the predicted toroidal shape because rather different decay geometries can produce elongated phase space distributions for the emitted particles. For example, the measured correlation functions for $P_{\text{lab}} = 400\text{-}600$ MeV/c could be rather well understood by assuming emission from a spherical source of finite lifetime [32]. In the future, more detailed investigations will have to clarify under which conditions more compelling experimental evidence for toroidal density distributions could be obtained and whether such signals survive when small, but non-zero impact-parameter collisions are admixed with weights reflecting realistic impact parameter filters. The identification of such observables goes beyond the purpose of the present investigation. Figure 11 serves as a reminder that the phase-space distribution of emitted particles is connected in a non-trivial way to the geometrical configuration of the source from which the particles are emitted.

Differences between longitudinal and transverse correlation functions caused by lifetime effects are best shown by defining the angle ψ in the rest frame of the emitting system [32]. For low-energy particles emitted in central collisions, the assumption of a source at rest in the center-of-momentum frame of projectile and target may be a reasonable simplification [32]. In less well defined situations, other directional dependencies may exist which may not be revealed by our choice of cuts on ψ . It is therefore instructive to explore angular cuts on ψ , defined in different rest frames and compare them to predictions of the BUU model.

The upper and lower panels in Figs. 12 and 13 show longitudinal (solid points) and transverse (open points) correlation functions with cuts on ψ defined in the laboratory and projectile rest frames, respectively. The right and left panels show data for the low and high momentum cuts, $P_{\text{lab}} = 400\text{-}600$ MeV/c and P_{lab}

= 700-1400 MeV/c, respectively. In Fig. 12, the data are compared with BUU predictions for the idealized case of $\hat{b} = 0$. In Fig. 13, they are compared to more realistic \hat{b} -selected calculations.

For the low momentum cut, $P_{\text{lab}} = 400\text{-}600$ MeV/c, the difference between longitudinal and transverse correlation functions becomes insignificant both when the cuts on ψ are applied in the laboratory frame (left, top panels in Figs. 12 and 13) and in the projectile rest frame (left, bottom panels). These trends are rather well reproduced by the BUU calculations, either using $b=0$ (Fig. 12) or realistic impact parameter weights according to the \hat{b} -selection technique (Fig. 13). For the present reaction, the emission of low-energy particles at large angles ($\theta_{\text{cm}} = 90^\circ$) appears to be rather well described by the BUU calculations, with little sensitivity to contributions from collisions at small, but non-zero impact parameter.

For the high momentum cut, $P_{\text{lab}} = 700\text{-}1400$ MeV/c, no significant difference between measured longitudinal and transverse correlation functions is observed when the cuts on ψ are applied in the laboratory frame (right, top panels in Figs. 12 and 13), but there is an indication for a small suppression of the transverse correlation function in the projectile rest frame (right, bottom panels). This difference is, however, of marginal statistical significance. These trends are reasonably well reproduced by the BUU calculations using $\hat{b} = 0$ (Fig. 12) which do, however, overpredict the magnitude of the peak at $q = 20$ MeV/c, as was already evident in Figs. 7-9. The \hat{b} -selected calculations (Fig. 13) predict a negligible difference between longitudinal and transverse correlation functions in the laboratory rest frame, in agreement with the experimental findings. In the projectile rest frame, however, these calculations predict a larger difference than observed experimentally, possibly indicating that the calculations predict

somewhat too large emission from projectile spectator matter than is observed experimentally.

In order to gain additional insight into the rest-frame dependence of longitudinal and transverse correlation functions predicted by BUU transport calculations, we plot in Fig. 14 the relative split, $\langle \Delta R \rangle / \langle R \rangle$, between longitudinal and transverse correlation functions calculated for specific impact parameters, $b = 0, 3, \text{ and } 6 \text{ fm}$, and for different rest frames of velocity $v_\psi = c\beta_\psi$ with respect to the laboratory system. ($\Delta R = R_{\text{long}} - R_{\text{trans}}$ is the difference between the longitudinal and transverse correlation functions evaluated in a given rest frame, R is the angle integrated correlation function which is independent of rest frame, and $\langle \rangle$ denotes the average value over the interval $15 \text{ MeV} \leq q \leq 40 \text{ MeV}$.) The top and bottom panels of Fig. 14, show the values of $\langle \Delta R \rangle / \langle R \rangle$ predicted for the cuts $P_{\text{lab}} = 400\text{-}600$ and $700\text{-}1400 \text{ MeV}/c$, respectively.

For the low-momentum cut, $P_{\text{lab}} = 400\text{-}600 \text{ MeV}/c$, the predictions for central collisions ($b = 0$, solid circles) follow the trends of the data: the largest value for $\langle \Delta R \rangle / \langle R \rangle$ is predicted in the center-of-momentum of projectile and target, and very small differences are predicted for longitudinal and transverse ψ -cuts defined in the target (laboratory) or projectile rest frames. A qualitative interpretation of this observation was given in ref. [32]. A very different behavior is predicted for a large ($b = 6 \text{ fm}$) impact parameter (open circular points). For such glancing collisions, no observable differences are predicted in the center-of-momentum frame. In contrast, significant differences are predicted when the ψ -cuts are defined in the target or projectile rest frames, consistent with the intuitive expectation that emission of mid-rapidity protons in peripheral

collisions is due to a superposition of emission from target and projectile-like sources.

For the high-momentum cut, $P_{\text{lab}} = 700\text{-}1400 \text{ MeV}/c$, differences between longitudinal and transverse correlation functions are predicted to be negligible for central ($b = 0 \text{ fm}$) collisions, independent of rest frame. These predictions follow the trends of the data. Fast particle emission in central collisions appears to occur on a fast time scale, and elongations of the phase-space distribution from finite-lifetime effects become negligible. For larger impact parameters, however, $\langle \Delta R \rangle / \langle R \rangle$ is predicted to become large for rest frame velocities close to the projectile velocity, indicating that fast, forward-emitted particles in peripheral collisions are predicted to have substantial (if not predominant) contributions from the decay of projectile residues. Note, however, that the BUU predictions for energetic emissions in peripheral collisions do not reproduce the data, see Fig. 7 and ref. [31]. Further, for peripheral cuts, no statistically significant differences between longitudinal and transverse correlation function were found experimentally in the target, projectile, nor in the center-of-momentum rest frames [32,51]. These findings corroborate that the details of proton emission in peripheral collisions are not well described by our calculations.

VIII. Conclusions

We measured two-proton correlation functions for $^{36}\text{Ar} + ^{45}\text{Sc}$ collisions at $E/A = 80 \text{ MeV}$, employing triple cuts on E_t (the transverse energy of associated charged particles), P_{lab} (the total momentum of the proton-pair), and ψ (the relative angle between total and relative momenta), and we compared the data to predictions of the BUU transport model.

The centrality of the experimental events was determined from the transverse energy, E_t , of associated charged particles detected in the 4π Array.

Since this quantity is not reproduced by BUU model calculations, due to the single-particle nature of the model, direct comparisons of impact-parameter selected data and to theoretical calculations are non-trivial. Two methods of selecting BUU events for comparison with impact-parameter selected data were employed. In the E_T -selection method, "equivalent- E_T " cuts [31] were applied to experimental and BUU events, and in the \hat{b} -selection method, "experimental" impact parameter distributions were used as input to the BUU. This latter method is computationally more efficient. Both methods give approximately the same results.

For central collisions, the BUU transport model describes the total momentum dependence of the angle-integrated correlation function quite well. It is then reasonable to assume that the space-time evolution of the proton-emitting zone generated in central collisions is also fairly well described by the theory. However, the BUU calculations fail to reproduce the total momentum dependence of the correlation function for peripheral events.

As a further test of the accuracy of the BUU transport model, we investigated longitudinal and transverse correlation functions for collisions at small impact parameters where predictions of the BUU model appear most accurate. Overall, the observed differences between longitudinal and transverse correlation functions were reproduced rather well by the BUU transport calculations with some slight disagreement emerging for the emission of high-energy protons when the longitudinal and transverse correlation functions were viewed in the projectile rest frame. These discrepancies could well arise from small admixtures of peripheral collisions for which the BUU predictions are less reliable.

Varying BUU parameters, such as the in-medium nucleon-nucleon cross section or the equation of state, may improve the agreement between predicted

and measured correlations and provide valuable physics information. It is likely that the theory's inability to form complex fragments plays an important role in causing the discrepancies between theory and experiment for peripheral collisions. This subject needs further experimental and theoretical study. Small additional theoretical uncertainties exist due to ambiguities in the criteria of when and where a particle is emitted. Finally, the discrepancies for modestly-peripheral collisions may indicate that the present model is incomplete in its description of such collisions and that it may be deficient in its description of surface effects. If so, the utility of the BUU in its present formulation may be limited to the description of very central collisions.

ACKNOWLEDGMENTS

This work was supported by the National Science Foundation under Grants No. PHY- 8913815, PHY-9017077, and PHY-9214992. One of us (W.B.) acknowledges support from a NSF Presidential Faculty Fellow Award.

References

1. S.E. Koonin, *Phys. Lett.* **70B**, 43 (1977).
2. D.H. Boal and J.C. Shillcock, *Phys. Rev.* **C33**, 549 (1986).
3. D.H. Boal and H. DeGuise, *Phys. Rev. Lett.* **57**, 2901 (1986).
4. S. Pratt and M.B. Tsang, *Phys. Rev.* **C36**, 2390 (1987).
5. W.G. Gong, W. Bauer, C.K. Gelbke, and S. Pratt, *Phys. Rev.* **C43**, 781 (1991).
6. D.H. Boal, C.K. Gelbke, and B.K. Jennings, *Rev. Mod. Phys.* **62**, 553 (1990).
7. W. Bauer, C.K. Gelbke, and S. Pratt, *Ann. Rev. Nucl. Part. Sci.* **42**, 77 (1992).
8. F. Zarbaksh, A.L. Sagle, F. Brochard, T.A. Mulera, V. Perez-Mendez, R. Talaga, I. Tanihata, J.B. Carroll, K.S. Ganezer, G. Igo, J. Oostens, D. Woodard, and R. Sutter, *Phys. Rev. Lett.* **46** 1268 (1981).
9. A. Kyanowski, F. Saint-Laurent, D. Ardouin, H. Delagrangé, H. Doubre, C. Grégoire, W. Mittig, A. Péghaire, J. Péter, Y.P. Viyogi, B. Zwiégliński, J. Québert, G. Bizard, F. Lefèbvres, B. Tamain, J. Pochodzalla, C.K. Gelbke, W. Lynch, and M. Maier, *Phys. Lett.* **B181**, 43 (1986).
10. H.A. Gustafsson, H.H. Gutbrod, B. Kolb, H. Loehner, B. Ludewigt, A.M. Poskanzer, T. Renner, H. Riedesel, H.G. Ritter, A. Warwick, F. Weik, and H. Wieman, *Phys. Rev. Lett.* **53**, 544 (1984).
11. W.G. Lynch, C.B. Chitwood, M.B. Tsang, D.J. Fields, D.R. Klesch, C.K. Gelbke, G.R. Young, T.C. Awes, R.L. Ferguson, F.E. Obenshain, F. Plasil, R.L. Robinson, and A.D. Panagiotou, *Phys. Rev. Lett.* **52**, 2302 (1984).
12. B. Erasmus, N. Carjan, and D. Ardouin, *Phys. Rev.* **C44**, 2663 (1991).

13. Z. Chen, C.K. Gelbke, J. Pochodzalla, C.B. Chitwood, D.J. Fields, W.G. Lynch, and M.B. Tsang, *Phys. Lett.* **B186**, 280 (1987).
14. D. Ardouin, P. Lautridou, D. Durand, D. Goujdami, F. Guilbault, C. Lebrun, A. Péghaire, J. Québert, and F. Saint-Laurent, *Nucl. Phys.* **A495**, 57c (1989).
15. P.A. DeYoung, C.J. Gelderloos, D. Kortering, J. Sarafa, K. Zienert, M.S. Gordon, B.J. Fineman, G.P. Gilfoyle, X. Lu, R.L. McGrath, D.M. de Castro Rizzo, J.M. Alexander, G. Auger, S. Kox, L.C. Vaz, C. Beck, D.J. Henderson, D.G. Kovar, and M.F. Vineyard, *Phys. Rev.* **C41**, R1885 (1990).
16. P.A. DeYoung, M.S. Gordon, Xiu qin Lu, R.L. McGrath, J.M. Alexander, D.M. de Castro Rizzo, and L.C. Vaz, *Phys. Rev.* **C39**, 128 (1989).
17. P. Dupieux, J.P. Alard, J. Augerat, R. Babinet, N. Bastid, F. Brochard, P. Charmensat, N. De Marco, H. Fanet, Z. Fodor, L. Fraysse, J. Girard, P. Gorodetzky, J. Gosset, C. Laspalles, M.C. Lemaire, D. L'Hôte, B. Lucas, J. Marroncle, G. Montarou, M.J. Parizet, J. Poitou, D. Qassoud, C. Racca, A. Rahmani, W. Schimmerling, and O. Vallete, *Phys. Lett.* **B200**, 17 (1988).
18. D. Fox, D.A. Cebra, J. Karn, C. Parks, A. Pradhan, A. Vander Molen, J. van der Plicht, G.D. Westfall, W.K. Wilson, and R.S. Tickle, *Phys. Rev.* **C38**, 146 (1988).
19. F. Zhu, W.G. Lynch, T. Murakami, C.K. Gelbke, Y.D. Kim, T.K. Nayak, R. Pelak, M.B. Tsang, H.M. Xu, W.G. Gong, W. Bauer, K. Kwiatkowski, R. Paneta, S. Rose, V.E. Viola, Jr., L.W. Woo, S. Yennello, and J. Zhang, *Phys. Rev.* **C44**, R582 (1991).
20. T.C. Awes, R.L. Ferguson, F.E. Obenshain, F. Plasil, G.R. Young, S. Pratt, Z. Chen, C.K. Gelbke, W.G. Lynch, J. Pochodzalla, H.M. Xu, *Phys. Rev. Lett.* **61**, (1988).

21. Z. Chen, C.K. Gelbke, W.G. Gong, Y.D. Kim, W.G. Lynch, M.R. Maier, J. Pochodzalla, M.B. Tsang, F. Saint-Laurent, D. Ardouin, H. Delegrange, H. Doubre, J. Kasagi, A. Kyanowski, A. Péghaire, J. Péter, E. Rosato, G. Bizard, F. Lefèbvres, B. Tamain, J. Québert, Y.P. Viyogi, *Phys. Rev. C* **36**, 2297 (1987).
22. Z. Chen, C.K. Gelbke, J. Pochodzalla, C.B. Chitwood, D.J. Fields, W.G. Gong, W.G. Lynch, and M.B. Tsang, *Nucl. Phys. A* **473**, 564 (1987).
23. J. Pochodzalla, C.K. Gelbke, W.G. Lynch, M. Maier, D. Ardouin, H. Delagrange, H. Doubre, C. Grégoire, A. Kyanowski, W. Mittag, A. Péghaire, J. Péter, F. Saint-Laurent, B. Zwieglinski, G. Bizard, F. Lefèbvres, B. Tamain, J. Québert, Y.P. Viyogi, W.A. Friedman, and D.H. Boal, *Phys. Rev. C* **35**, 1695 (1987).
24. W.G. Gong, C.K. Gelbke, N. Carlin, R.T. de Souza, Y.D. Kim, W.G. Lynch, T. Murakami, G. Poggi, D. Sanderson, M.B. Tsang, H.M. Xu, D.E. Fields, K. Kwiatkowski, R. PJaneta, V.E. Viola, Jr., S.J. Yennello, and S. Pratt, *Phys. Lett. B* **246**, 21 (1990).
25. W.G. Gong, W. Bauer, C.K. Gelbke, N. Carlin, R.T. de Souza, Y.D. Kim, W.G. Lynch, T. Murakami, G. Poggi, D. Sanderson, M.B. Tsang, H.M. Xu, S. Pratt, D.E. Fields, K. Kwiatkowski, R. PJaneta, V.E. Viola, Jr., and S.J. Yennello, *Phys. Rev. Lett.* **65**, 2114 (1990).
26. W.G. Gong, C.K. Gelbke, W. Bauer, N. Carlin, R.T. de Souza, Y.D. Kim, W.G. Lynch, T. Murakami, G. Poggi, D. Sanderson, M.B. Tsang, H.M. Xu, D.E. Fields, K. Kwiatkowski, R. PJaneta, V.E. Viola, Jr., S.J. Yennello, and S. Pratt, *Phys. Rev. C* **43**, 1804 (1991).
27. J. Pochodzalla, C.B. Chitwood, D.J. Fields, C.K. Gelbke, W.G. Lynch, M.B. Tsang, D.H. Boal, and J.C. Shillcock, *Phys. Lett. B* **174**, 36 (1986).

28. W.G. Lynch, C.B. Chitwood, M.B. Tsang, D.J. Fields, D.R. Klesch, C.K. Gelbke, G.R. Young, T.C. Awes, R.L. Ferguson, F.E. Obenshain, F. Plasil, R.L. Robinson, and A.D. Panagiotou, *Phys. Rev. Lett.* **51**, 1850 (1983).
29. D. Goujdami, F. Guilbault, C. Lebrun, D. Ardouin, H. Dabrowski, S. Pratt, P. Lautridou, R. Boisgard, J. Québert, and A. Péghaire, *Z. Phys.* **A339**, 293 (1991).
30. G.J. Kunde, J. Pochodzalla, E. Berdermann, B. Berthier, C. Cerruti, C.K. Gelbke, J. Hubele, P. Kreuzt, S. Leray, R. Lucas, U. Lynen, U. Milkau, C. Ngô, C.H. Pinkenburg, G. Raciti, H. Sann, and W. Trautmann, *Phys. Rev. Lett.* **70**, 2545 (1993).
31. M.A. Lisa, C.K. Gelbke, W. Bauer, P. Decowski, W.G. Gong, E. Gualtieri, S. Hannuschke, R. Lacey, T. Li, W.G. Lynch, C.M. Mader, G.F. Peaslee, T. Reposeur, A.M. Vander Molen, G.D. Westfall, J. Yee, and S.J. Yennello, *Phys. Rev. Lett.* **70**, 3709 (1993).
32. M.A. Lisa, C.K. Gelbke, W. Bauer, P. Decowski, W.G. Gong, E. Gualtieri, S. Hannuschke, R. Lacey, T. Li, W. G. Lynch, C.M. Mader, G.F. Peaslee, S. Pratt, T. Reposeur, A.M. Vander Molen, G.D. Westfall, J. Yee, and S.J. Yennello, *Phys. Rev. Lett.* **71**, 2863 (1993).
33. D. Rebreyend, F. Merchez, B. Norén, E. Andersen, M. Cronqvist, J. C. Gondrand, H. A. Gustafsson, B. Jäger, B. Jakobsson, B. Khelifaouli, S. Kox, A. Kristiansson, G. Lövhöiden, S. Mattson, T. F. Thorsteinsen, M. Westenius, and L. Westerberg, *Phys. Rev.* **C46**, 2387 (1992).
34. M. Korolija, D. Shapira, J. Gomes del Campo, E. Chavez, and N. Cindro, *Phys. Rev.* **C49**, 272 (1994).

35. G.D. Westfall, J.E. Yurkon, J. van der Plicht, Z.M. Koenig, B.V. Jacak, R. Fox, G.M. Crawley, M.R. Maier, and B.E. Hasselquist, *Nucl. Instr. and Meth.* **A238**, 347 (1985).
36. W.G. Gong, Y.D. Kim, G. Poggi, Z. Chen, C.K. Gelbke, W.G. Lynch, M.R. Maier, T. Murakami, M.B. Tsang, H.M. Xu, and K. Kwiatkowski, *Nucl. Instr. and Meth.* **A268**, 190 (1988).
37. W.G. Gong, N. Carlin, C.K. Gelbke, and R. Dayton, *Nucl. Instr. and Meth.* **A287**, 639 (1990).
38. L. Phair, D.R. Bowman, C.K. Gelbke, W.G. Gong, Y.D. Kim, M.A. Lisa, W.G. Lynch, G.F. Peaslee, R.T. de Souza, M.B. Tsang, and F. Zhu, *Nucl. Phys.* **A548**, 489 (1992).
39. L. Phair, D.R. Bowman, N. Carlin, C.K. Gelbke, W.G. Gong, Y.D. Kim, M.A. Lisa, W.G. Lynch, G.F. Peaslee, R.T. de Souza, M.B. Tsang, C. Williams, F. Zhu, N. Colonna, K. Hanold, M.A. McMahan, and G.J. Wozniak, *Nucl. Phys.* **A564**, 453 (1993).
40. W. Bauer, G.F. Bertsch, W. Cassing, and U. Mosel, *Phys. Rev.* **C34**, 2127 (1986).
41. W. Bauer, *Nucl. Phys.* **A471**, 604 (1987).
42. B.A. Li and W. Bauer, *Phys. Rev.* **C44**, 450 (1991).
43. B.A. Li, W. Bauer, and G.F. Bertsch, *Phys. Rev.* **C44**, 2095 (1991).
44. M.A. Lisa, W.G. Gong, C.K. Gelbke, and W.G. Lynch, *Phys. Rev.* **C44**, 2865 (1991).
45. D. Klakow, G. Welke, and W. Bauer, *Phys. Rev.* **C48**, 1982 (1993).

46. Y.D. Kim, R.T. de Souza, C.K. Gelbke, W.G. Gong, and S. Pratt, *Phys. Rev. C* **45**, 387 (1992).
47. L.G. Moretto, K. Tso, N. Colonna, and G.J. Wozniak, *Phys. Rev. Lett.* **69**, 1884 (1992).
48. W. Bauer, G.F. Bertsch, and H. Schulz, *Phys. Rev. Lett.* **69**, 1888 (1992).
49. B.A. Li and D.H.E. Gross, *Nucl. Phys. A* **554**, 257 (1993).
50. H.M. Xu, J.B. Natowitz, C.A. Gagliardi, R.E. Tribble, C.Y. Wong, and W.G. Lynch, *Phys. Rev. C* **48**, 933 (1993).
51. M.A. Lisa, Ph.D. Thesis, Michigan State University (1993).

Figure Captions

Figure 1: Angular coverage of the 56-element high-resolution hodoscope. Each telescope covered about 0.37 msr in solid angle.

Figure 2: Upper panel: transverse energy distribution, dP/dE_t , measured for a minimum bias trigger. Lower panel: average reduced impact parameter scale derived with Eq. 1.

Figure 3: Reduced impact parameter distributions determined with Eq. 1 as discussed in the text. The solid line (linear by construction) represents the minimum bias trigger. The dot-dashed and dashed curves represent distributions for single and two-proton inclusive events detected in the 56-element hodoscope. These events show a distinct bias toward smaller impact parameters.

Figure 4: Total transverse energy spectrum, dP/dE_t , measured with the minimum bias trigger (solid line). Also plotted are predictions of the BUU model, after passing through the detector acceptance of the 4π array. Calculations of E_t which include contributions from all emitted nucleons are shown by the dashed line, those including only protons are shown by the dot-dashed line. Relative normalizations are adjusted to give equal areas for $E_t > 100$ MeV.

Figure 5: Reduced impact parameter distributions $dP/d\hat{b}(E_t)$ for the narrow cuts on $\hat{b}(N_C)$ and $\hat{b}(Z_Y)$ indicated in the figure. The upper and lower panels show $dP/d\hat{b}(E_t)$ for central and mid-central cuts on $\hat{b}(N_C)$ and $\hat{b}(Z_Y)$.

Figure 6: Upper Panel: Sharp cuts on $\hat{b}(E_t)$ used to define central and peripheral events. Lower Panel: Distributions, $dP/d\hat{b}_{true}$, of the "true" reduced impact parameter corresponding to the cuts on $\hat{b}(E_t)$ shown in the upper panel.

Figure 7: Average height of the correlation function in the region $15 \text{ MeV}/c \leq q \leq 25 \text{ MeV}/c$ as a function of the total laboratory momentum of the proton pairs,

P_{lab} . The right-hand axis gives the source radius of a zero- lifetime spherical source with a Gaussian density profile that would produce a correlation of equal magnitude. The upper and lower panels show results for central and peripheral events. Data are shown by solid circles. BUU predictions are displayed by open symbols and solid diamonds. The lines are drawn to guide the eye. Error bars on the data points include statistical errors as well as uncertainties in normalizing the correlation function at large q . Error bars for BUU predictions were obtained by comparing the variations between predictions for $\langle 1+R \rangle_{15-25\text{MeV}/c}$ from three independent ensembles of events. Further details are given in the text.

Figure 8: Solid and open points show longitudinal and transverse correlation functions measured for central collisions at the indicated momenta. The curves show BUU predictions for the idealized case of purely central collisions ($b=0$). The cuts on ψ were performed in the center-of-momentum frame of projectile and target.

Figure 9: Solid and open points show longitudinal and transverse correlation functions measured for central collisions at the indicated momenta. The curves show BUU predictions employing the \hat{b} -selection method explained in the text. The cuts on ψ were performed in the center-of-momentum frame of projectile and target.

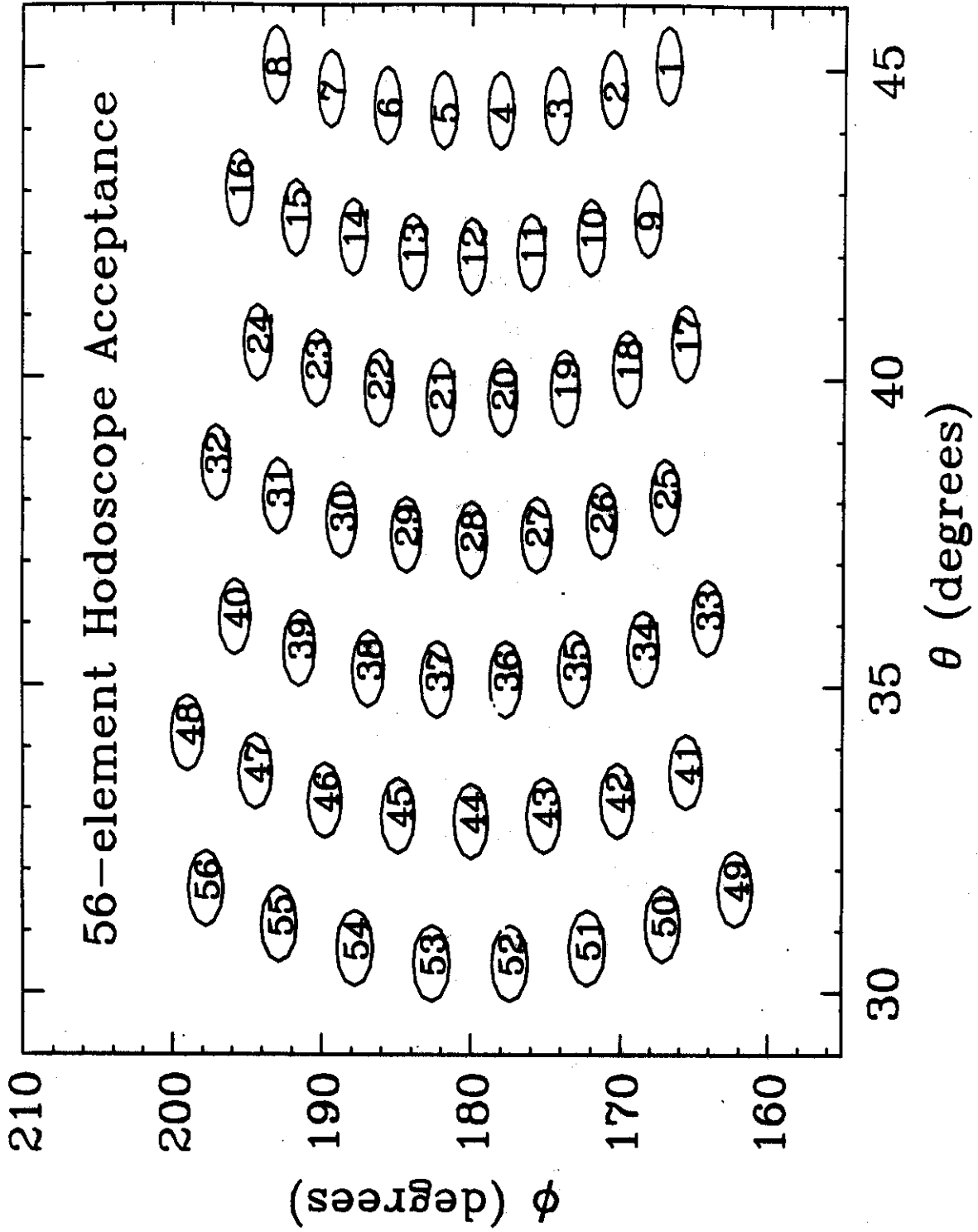
Figure 10: Schematic of detector acceptance and momentum cuts. Dashed lines represent the detector boundaries at $\theta_{lab} = 30^\circ - 45^\circ$. Dotted and hatched areas represent the low and high momentum cuts, $P_{lab} = 400-600$ and $700-1400$ MeV/c, respectively. Solid circles depict Fermi spheres of target and projectile; dashed circle illustrates a "mid-rapidity" source representing momenta accessible by single nucleon-nucleon scattering processes.

Figure 11: Center-of-mass coordinates of phase space points predicted by BUU at four time steps: $t=0, 50, 100,$ and 150 fm/c. Points representing particles of momentum $p_{lab} = 195-205$ MeV/c, emitted into the angular acceptance of the hodoscope, are plotted as light dots. "Source points" representing the residual system are shown by heavy dots. All points displayed are selected by the cut $|y| < 3$ fm. The residual system evolves into a relatively long-lived toroidal object, represented by two circular regions to the left and right of the beam axis. The emission points produce a "cloud," elongated in the direction of motion (indicated by the arrows) toward the detector, located at $\theta_{cm} \approx 97^\circ$.

Figure 12: Longitudinal (solid points and curves) and transverse (open points and dashed curves) correlation functions constructed in the laboratory (top) and projectile (bottom) rest frames. Left and right panels show results for low and high momentum cuts, respectively. Points show data selected by the central cut, $\hat{b} < 0.36$. The curves show BUU predictions for $\hat{b} = 0$.

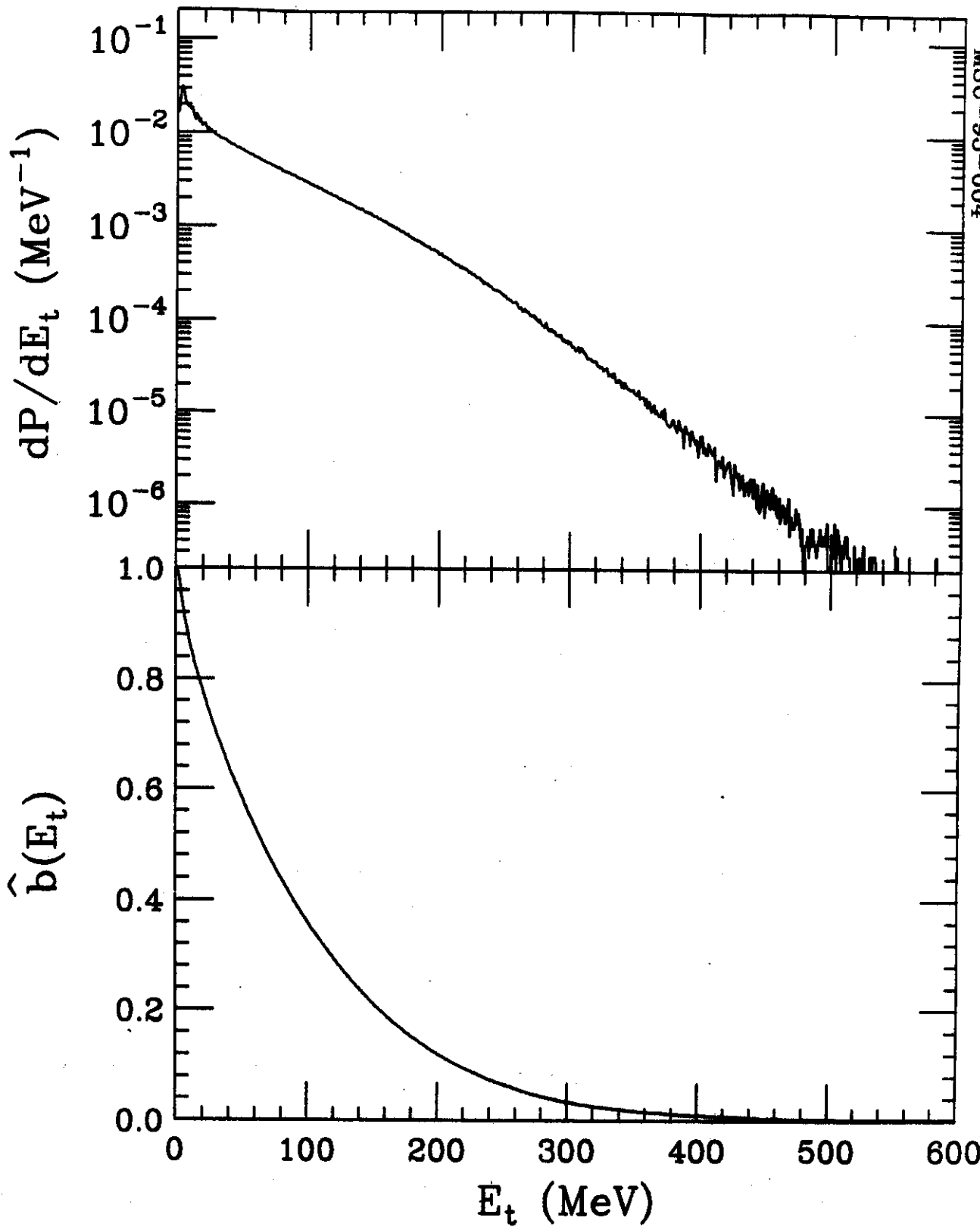
Figure 13: Longitudinal (solid points and curves) and transverse (open points and dashed curves) correlation functions constructed in the laboratory (top) and projectile (bottom) rest frames. Left and right panels show results for low and high momentum cuts, respectively. Points show data selected by the central cut, $\hat{b} < 0.36$. The curves show BUU predictions with the \hat{b} -selection technique.

Figure 14: Relative difference, $\langle \Delta R \rangle / \langle R \rangle$, between longitudinal and transverse correlation functions as a function of the velocity, β_{ψ} , of the rest frame in which the longitudinal and transverse ψ -cuts are defined. Shown are BUU predictions for $b=0$ (solid circles), $b=3$ fm (open diamonds), and $b=6$ fm (open circles). Results for low and high momentum cuts are displayed in the upper and lower panels, respectively.

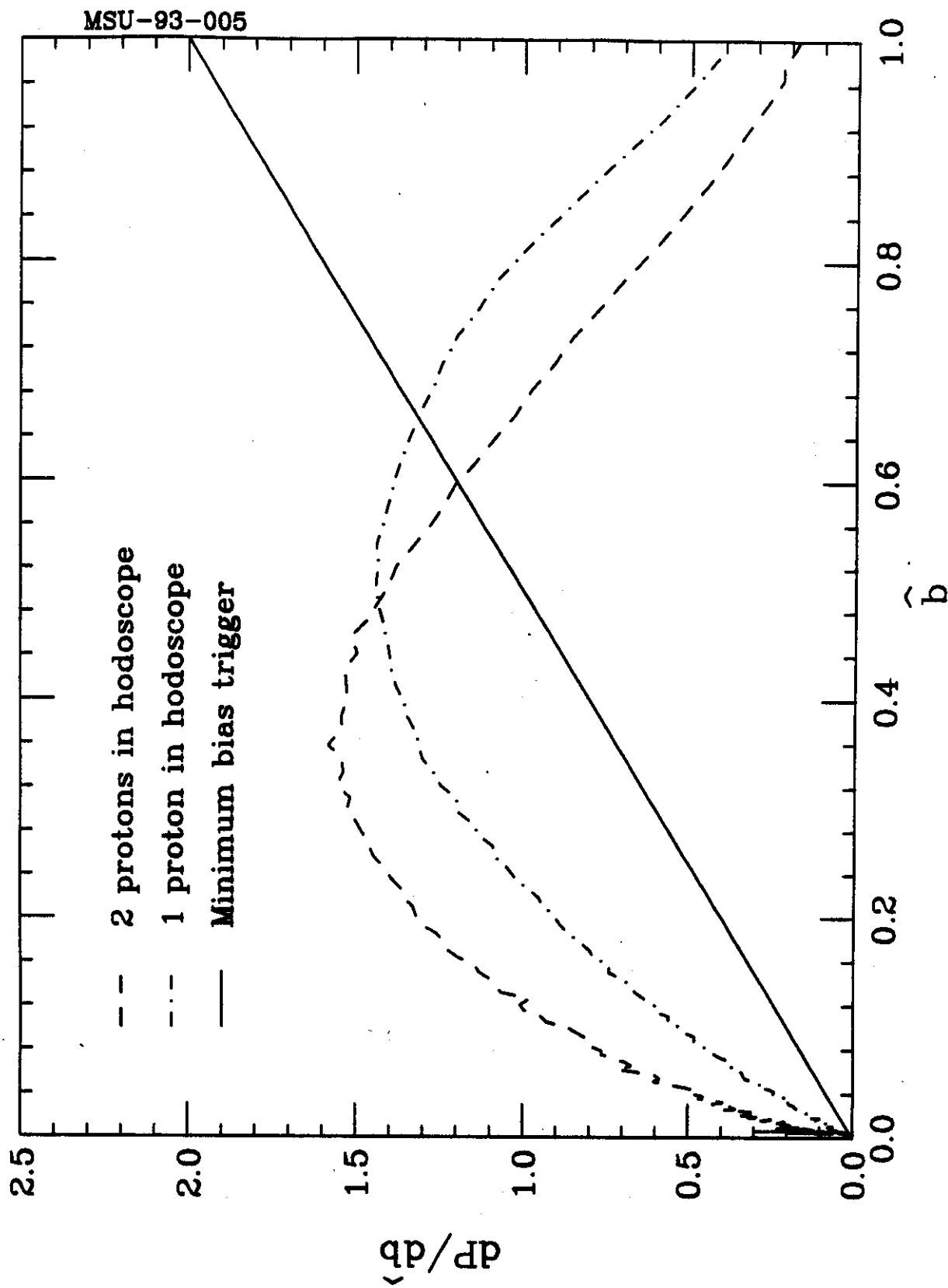


D.O. Handzy et. al. Figure 1

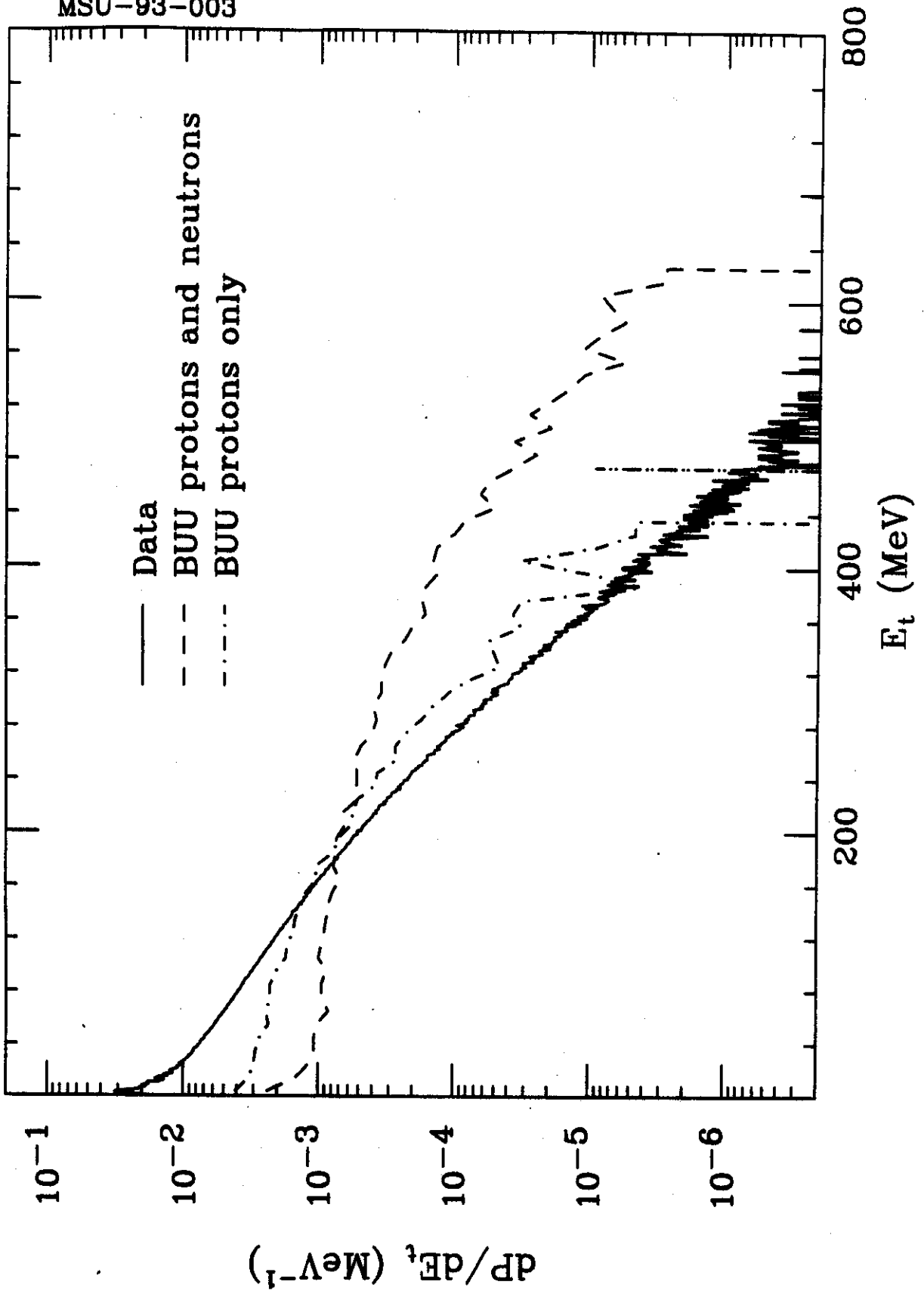
MSU-93-004



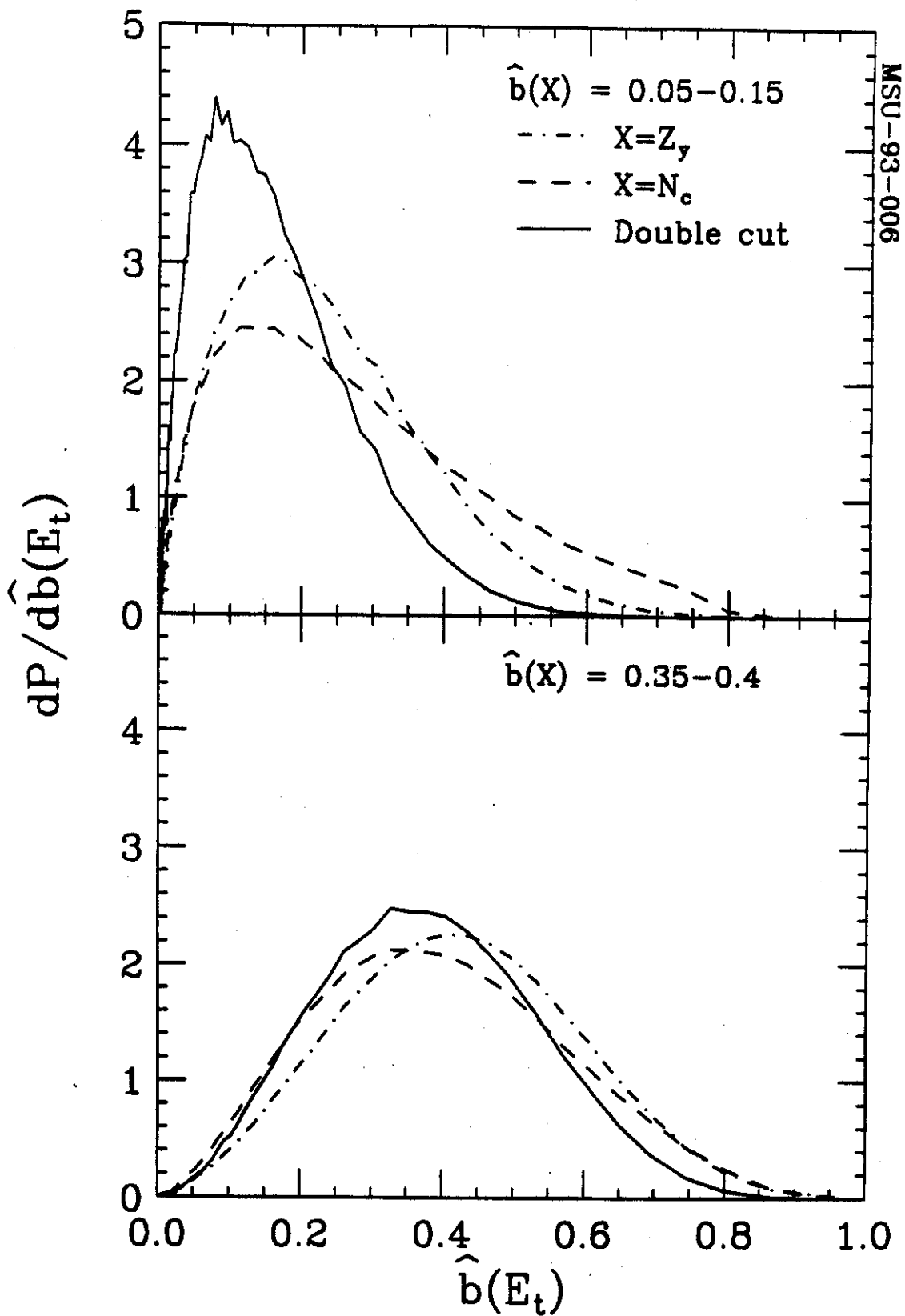
D.O. Handsy et. al. Figure 2



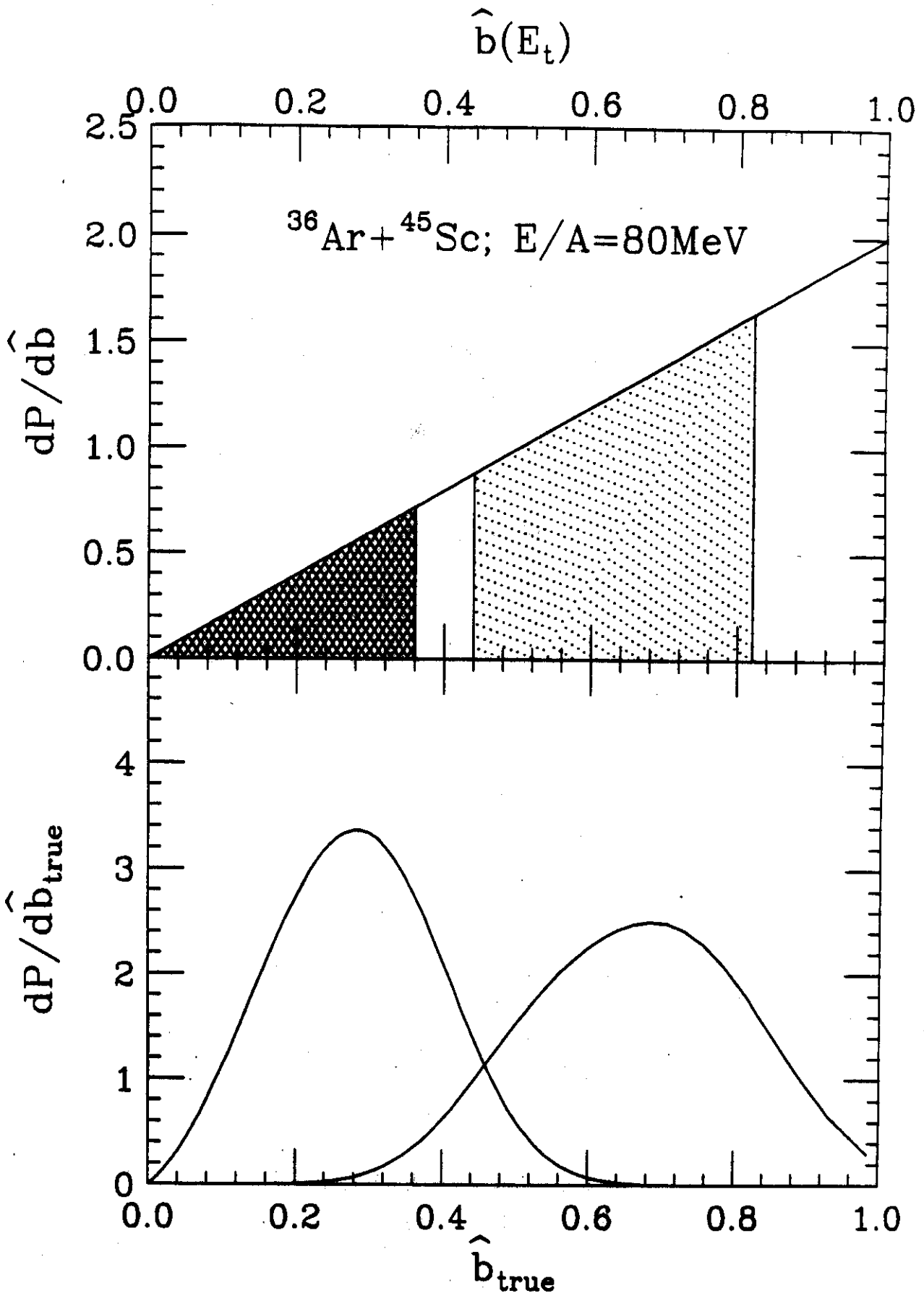
MSU-93-003



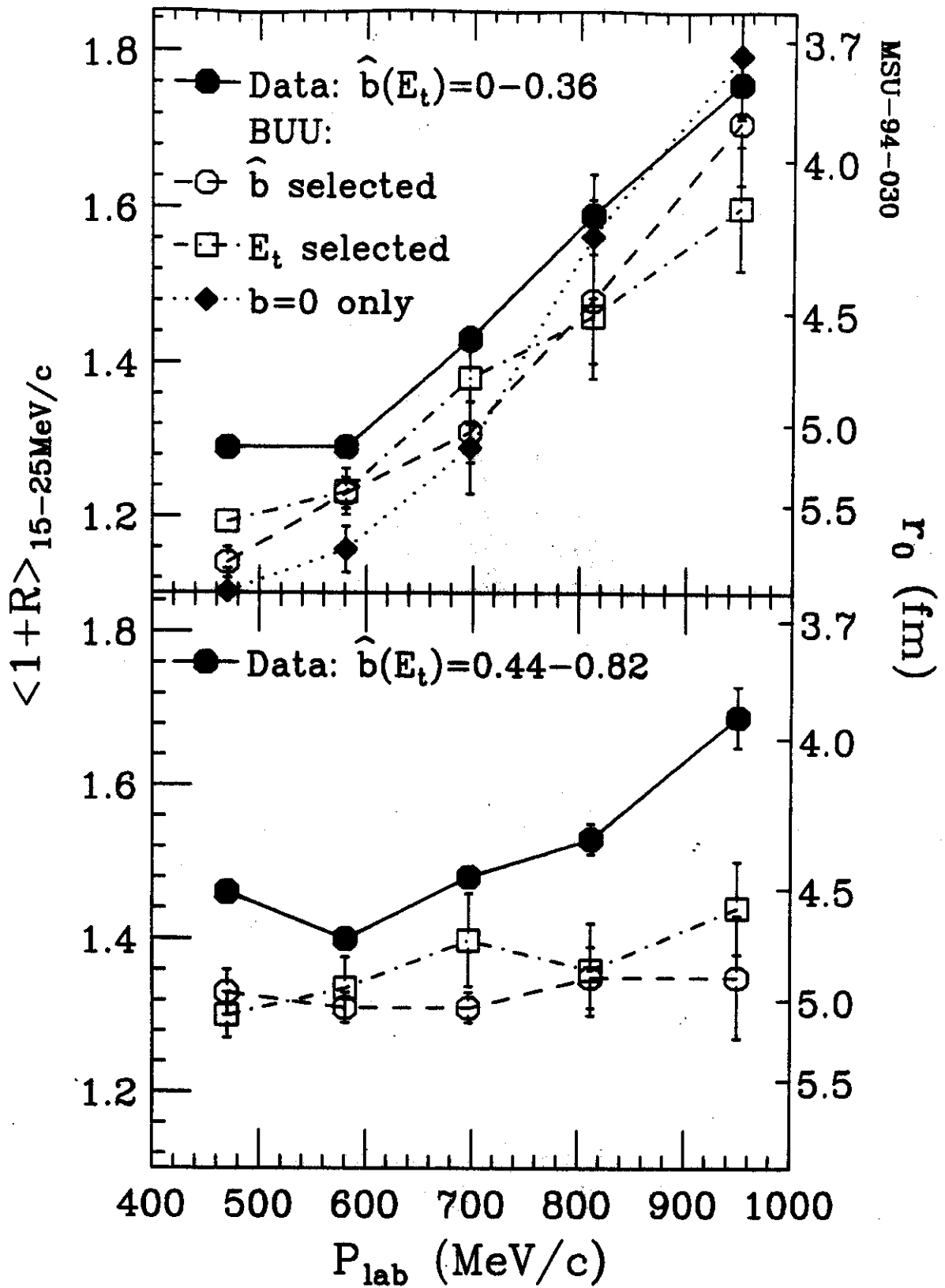
D.O. Handzy et. al. Figure 4

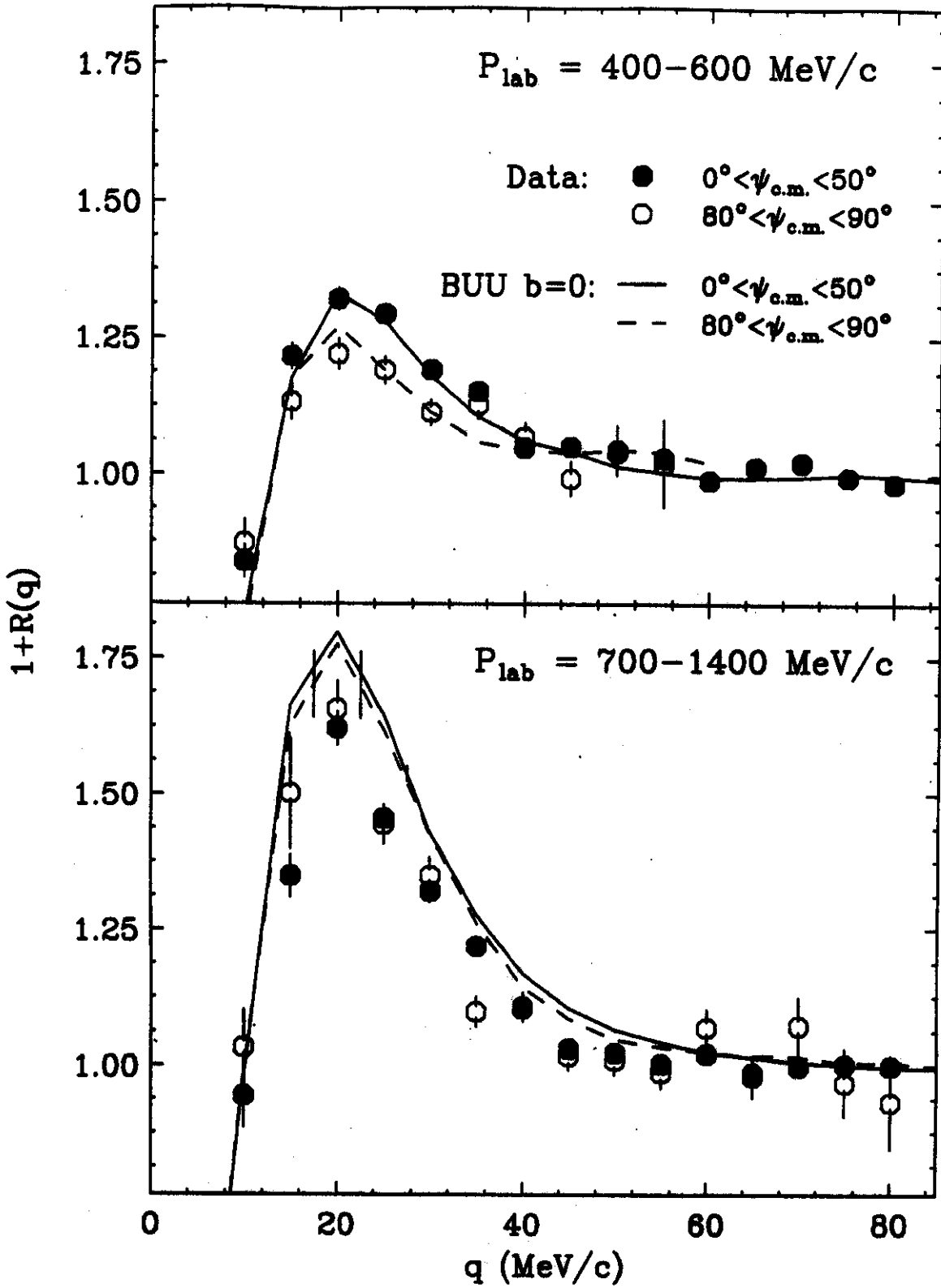


D.O. Handzy et. al. Figure 5

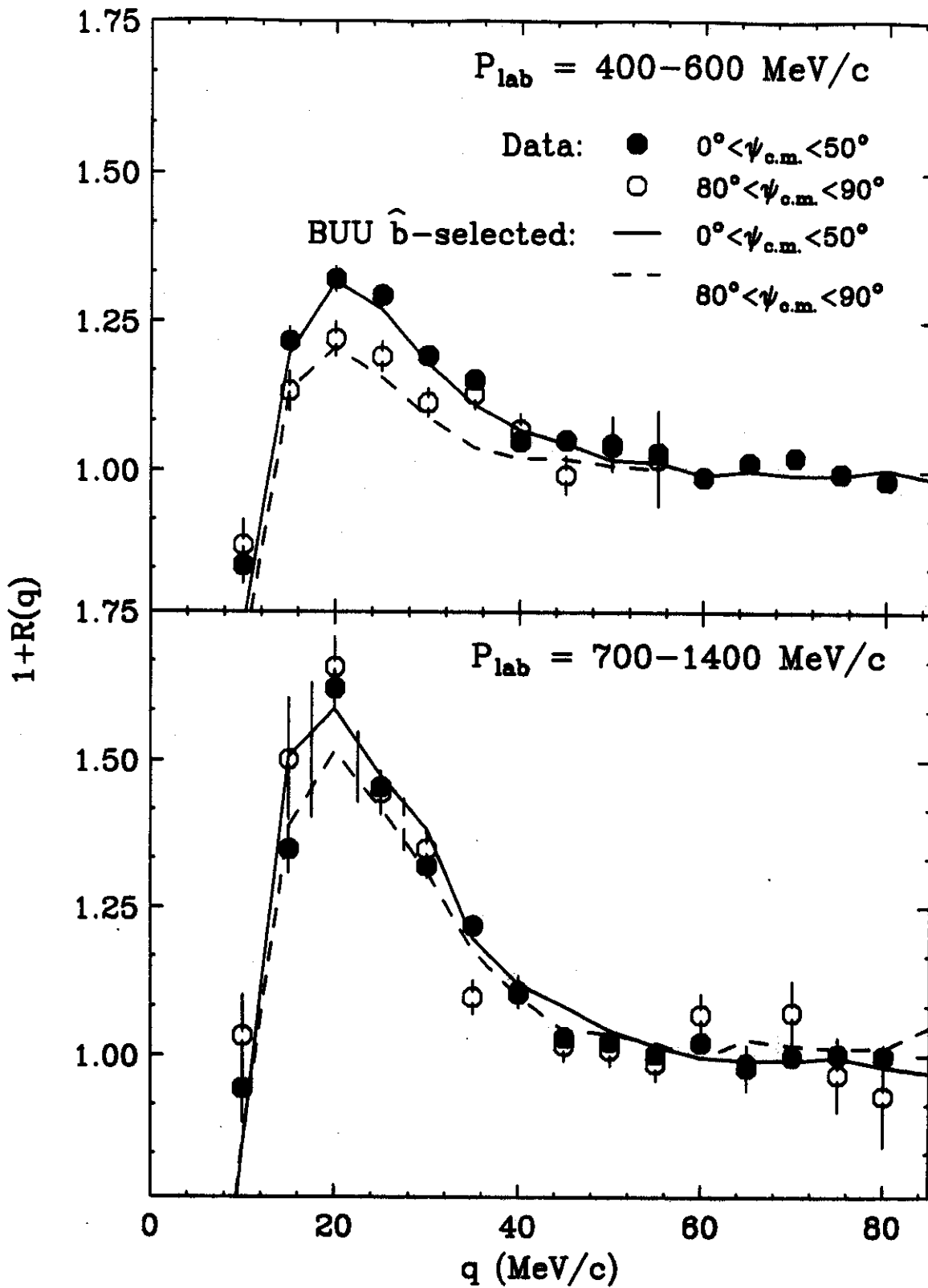


D.O. Handsy et. al. Figure 6

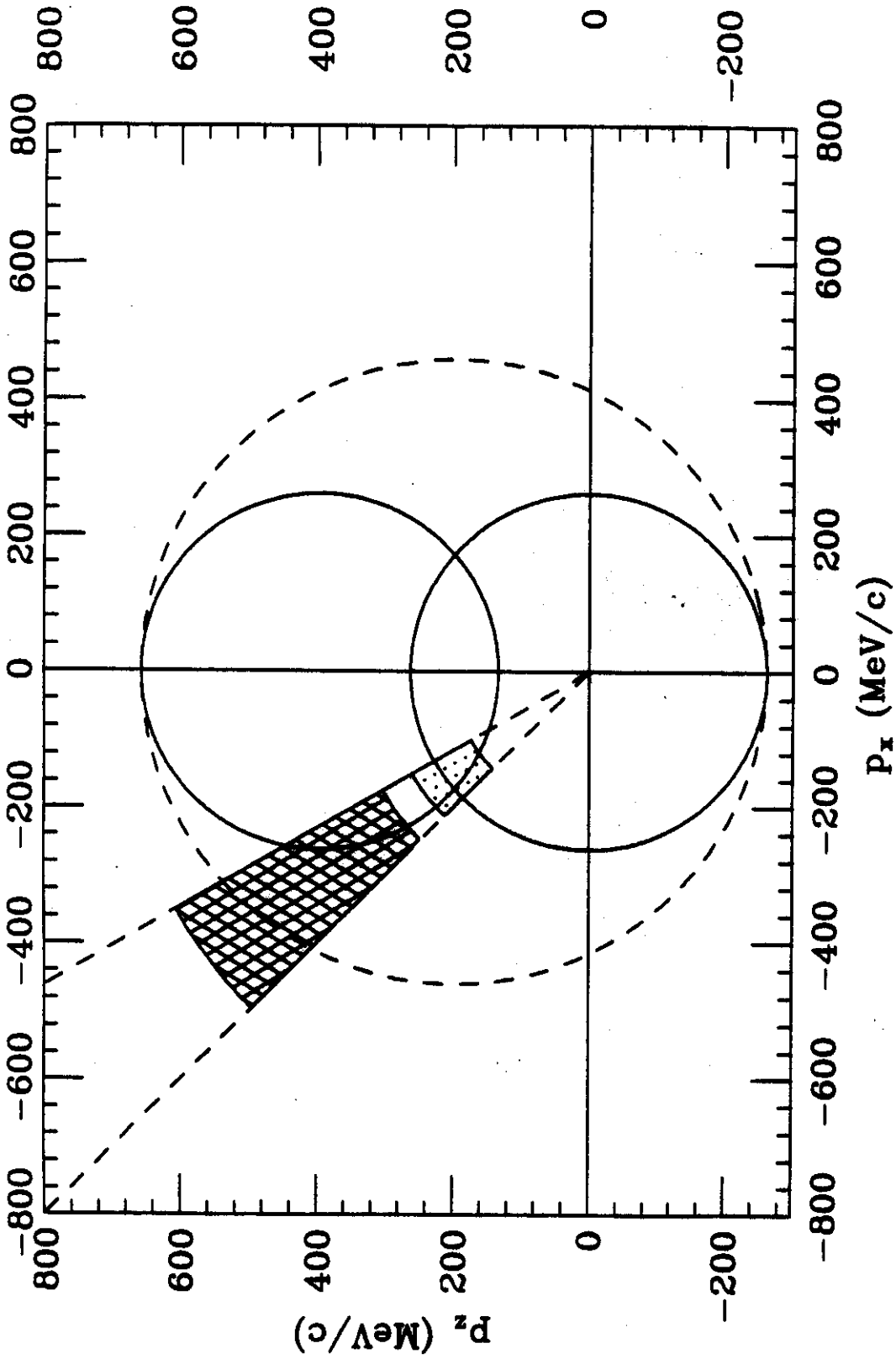




D.O. Handzy et. al. Figure 8

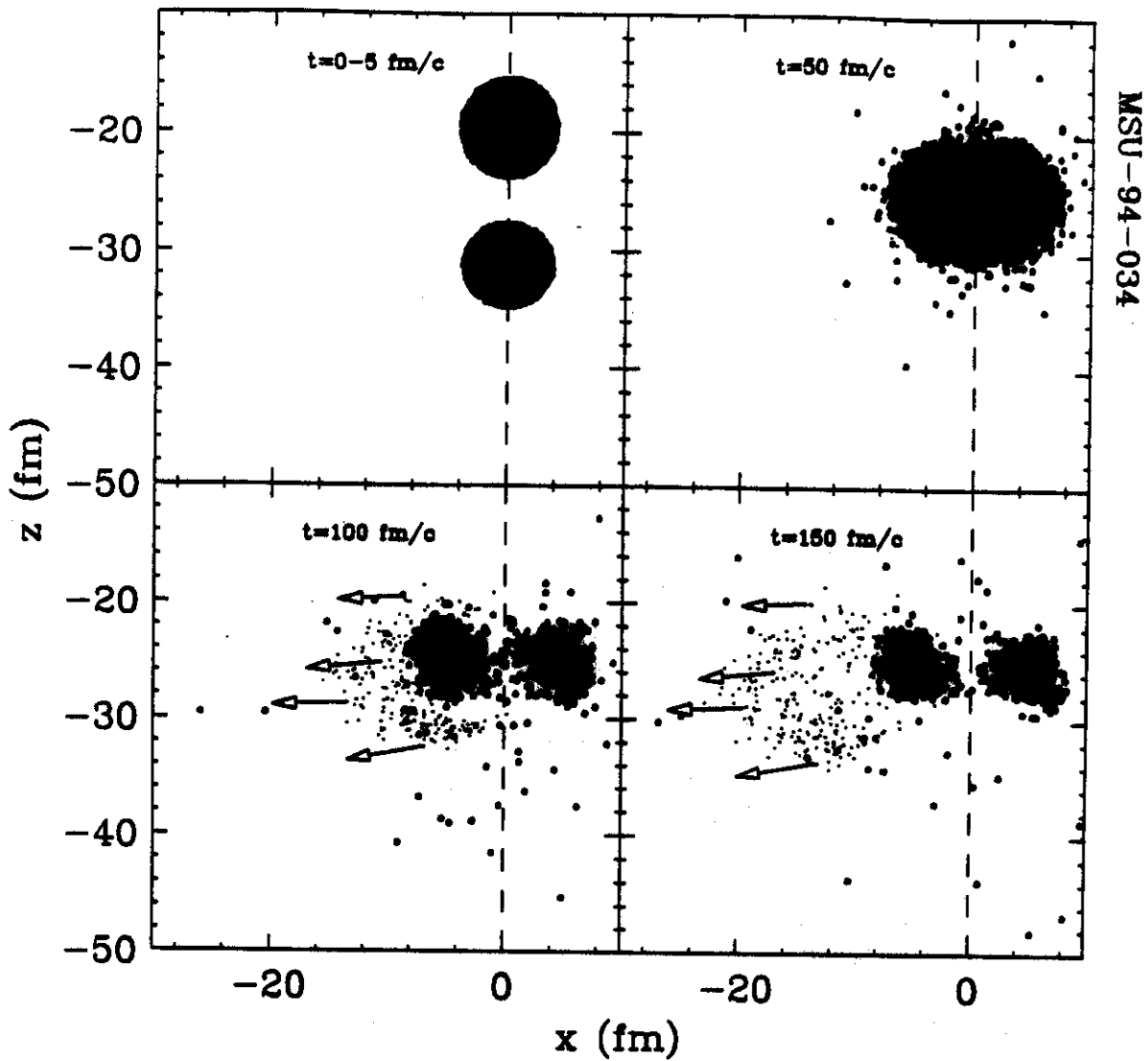


MSU-94-033



D.O. Handzy et. al. Figure 10

BUU: $^{36}\text{Ar} + ^{45}\text{Sc}$; $E/A = 80$ MeV



D.O. Handzy et. al Figure 11

